catalysts

MDPI

Article

Rendering Visible-Light Photocatalytic Activity to Undoped ZnO via Intrinsic Defects Engineering

Lan-li Chen [1], Bao-gai Zhai [2] and Yuan Ming Huang [2,*]

[1] School of Mathematics and Physics, Nanyang Institute of Technology, Nanyang 473004, China; 3032014@nyist.edu.cn

[2] School of Microelectronics and Control Engineering, Changzhou University, Changzhou 213164, China; bgzhai@cczu.edu.cn

* Correspondence: ymhuang@cczu.edu.cn

Received: 2 September 2020; Accepted: 8 October 2020; Published: 11 October 2020

Abstract: It is significant to render visible-light photocatalytic activity to undoped ZnO nanostructures via intrinsic defect engineering. In this work, undoped ZnO nanocrystals were derived via co-precipitation synthesis. The resulting ZnO nanocrystals were characterized by means of X-ray diffraction, scanning electron microscopy, photoluminescence spectroscopy, and ultraviolet-visible absorption spectroscopy, respectively. The visible-light photocatalytic activity of the products were characterized by monitoring the decomposition of methyl orange in water under visible-light illumination of a 300 W halogen lamp. It is found that undoped ZnO nanocrystals exhibit visible-light photocatalytic activity with their first-order rate constant up to 4.6×10^{-3} min^{-1}. Density functional calculations show that oxygen vacancies create deep energy levels at E_V + 0.76 eV in the bandgap of ZnO. In conjunction with the density functional calculations, the photocatalytic degradation of methyl orange under visible-light irradiation provides direct evidence that oxygen vacancies in ZnO nanocrystals yield the visible-light photocatalytic activity. Our results demonstrate that visible-light photocatalytic activity can be endowed to undoped ZnO nanocrystals by manipulating the intrinsic defects in ZnO. Intrinsic defect-modulated ZnO photocatalysts thus represent a powerful configuration for further development toward visible-light responsive photocatalysis.

Keywords: undoped ZnO; visible-light photocatalytic activity; intrinsic defect; oxygen vacancy

1. Introduction

The increase in hazardous organic pollution generates high demand for ecologically clean solutions. Being able to use the abundant solar light, semiconductor photocatalysis is one of the most promising solutions to decomposing numerous organic pollutants in water [1,2]. Among the diverse semiconductors, ZnO nanocrystals have attracted a lot of attention because of their advantages of suitable energy band positions, low toxicity, and high chemical stability [3–6]. However, it is a general belief that perfect ZnO cannot exhibit visible-light photocatalytic activity since the bandgap of perfect ZnO is too large (3.37 eV). To harness the visible irradiation from the Sun, defect engineering is often employed to regulate the band structures of ZnO. For example, doping ZnO with transitional elements can create midgap states in the bandgap of ZnO, thereby rendering ZnO with visible-light photocatalytic activity by shifting its optical absorption to the visible spectral regime [7–15].

Aside from doping with extrinsic defects, ZnO nanostructures are rich in intrinsic defects [16–18]. The absorption properties of ZnO can be largely affected by both extrinsic dopants and native defects. Theoretically speaking, these intrinsic defects can make ZnO absorb photons in the visible-light spectral regime by generating defect energy levels in the bandgap of ZnO. In this way, ZnO nanostructures bearing these intrinsic defects can display excellent visible-light photocatalytic activities. Indeed,

Hamdy et al. reported that oxygen-defected ZnO tetrapods exhibited higher activity than ZnO tetrapods under the illumination of 425 ± 20 nm [19]; Wang et al. reported that defect-rich ZnO nanosheets showed visible-light photocatalytic activity under visible-light illumination λ > 420 nm [20]. When compared to transitional metals doped ZnO, the intrinsic defects incurred visible-light photocatalytic activity of ZnO has not received substantial interest, leaving some fundamental questions unanswered: (i) the defect energy levels of oxygen vacancies are not provided for ZnO; (ii) the contributions of other intrinsic defects such as zinc vacancies to the visible-light photocatalytic activity of undoped ZnO are not taken into consideration; and (iii) the quantitative relationship between the defect energy levels of oxygen vacancies and the visible-light photocatalytic activity of undoped ZnO is not firmly established. Therefore further investigations are required to provide information on the defect energy levels of oxygen and zinc vacancies in the bandgap of ZnO so that a reliable relationship between the defect energy levels of intrinsic defects and the visible-light photocatalytic activity can be established for undoped ZnO.

In this work, we aim to study the intrinsic defects incurred visible-light photocatalytic activity of undoped ZnO under the visible-light illumination of a 300 W halogen lamp. Density functional calculations demonstrate that the visible-light photocatalytic activity of undoped ZnO nanocrystals is associated with the oxygen vacancies in the lattice of ZnO. Moreover, we analyzed the visible-light photocatalytic activity of undoped ZnO nanocrystals subject to thermal annealing at temperatures in the range of 100–300 °C. It was found that the visible-light photocatalytic activity of annealed ZnO nanocrystals was heavily dependent on the annealing temperature. In addition to establishing the relationship between the intrinsic defects in undoped ZnO and its visible-light photocatalytic activity, this work offers a new strategy for rendering ZnO with visible-light responsive photocatalytic activity via intrinsic defect modulation.

2. Results and Discussions

2.1. Morphology and Crystal Structure of ZnO Nanocrystals

The powder X-ray diffraction (XRD) curve of undoped ZnO nanocrystals is shown in Figure 1. The open circles in Figure 1 represent the raw data. As shown in Figure 1, the undoped ZnO nanocrystals show diffraction peaks at 31.74, 34.40, 36.22, 47.48, 56.56 and 62.80°, respectively. These peaks can be assigned to the reflections from the (100), (002), (101), (102), (110) and (103) planes of hexagonal ZnO (Joint Committee on Powder Diffraction Standards card no. 36–1451), as discussed in previous work [3–5,12,16,17]. Apparently, the diffraction peaks in Figure 1 agree well with those of wurtzite ZnO. The lattice constants of the perfect wurtzite ZnO nanocrystals are known to be a = 0.32498 nm and c = 0.52066 nm. In order to obtain any sensible estimates of the lattice parameters, Rietveld refinement was performed for the undoped ZnO nanocrystals. The solid green curve in Figure 1 represents the calculated diffractogram using Rietveld refinement. On the basis of Rietveld refinement, the lattice parameters of the ZnO nanocrystals are derived as a = 0.32499 nm and c = 0.52061 nm. The standard deviations of a and c are 0.00011 nm and 0.00017 nm, respectively. Obviously, the data in Figure 1 have confirmed the wet chemistry synthesis results in wurtzite ZnO.

Figure 2 illustrates the scanning electron microscope (SEM) micrograph (a) and the low-magnification transmission electron microscope (TEM) micrograph (b) of undoped ZnO nanocrystals. Obviously, the ZnO nanocrystals are in the shape of spheres. Generally speaking, sphere-like ZnO nanocrystals often result from the wet-chemical techniques when polar surfactants (such as hexamethylenetetramine) are absent in the reaction liquids [8,9,12]. Otherwise, rod-like or disk-like ZnO microstructures can occur when polar surfactants are present in the reaction liquids [7,13]. Since the photocatalytic activity of a photocatalyst is heavily dependent on its crystal size, information on the crystal sizes of ZnO nanocrystals is critically important. As can be seen in Figure 2b, the diameter of undoped ZnO nanocrystals ranges from 30 to 80 nm with a mean diameter value of approximately 50 nm. Additionally, the specific surface area of the undoped ZnO nanocrystals was analyzed using

the Brunauer-Emmett-Teller (BET) gas adsorption method using a Micromeritics Tristar 3000 system. The BET surface of the undoped ZnO nanocrystals was measured to be about 6.9 m^2/g.

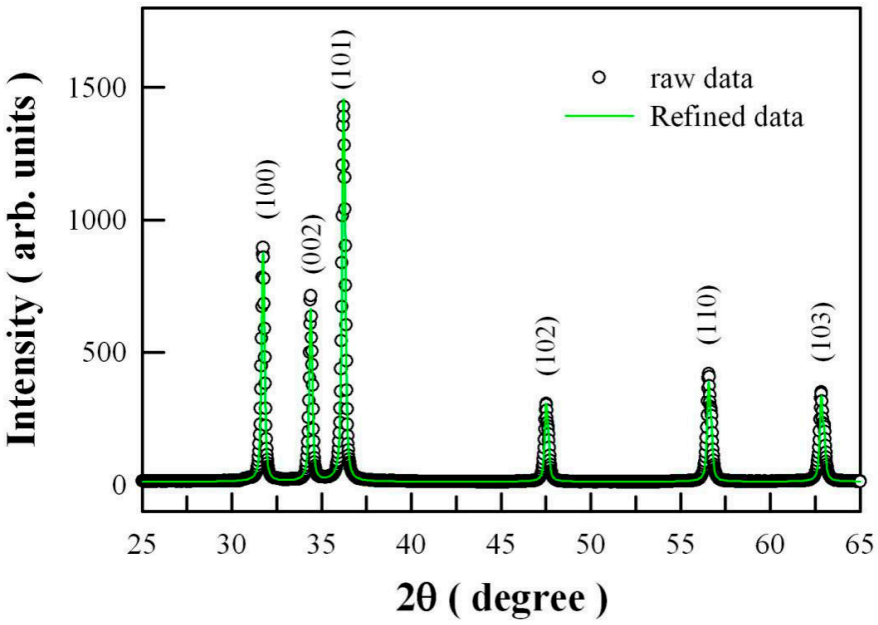

Figure 1. X-ray diffraction (XRD) curve of undoped ZnO nanocrystals and its Rietveld analysis.

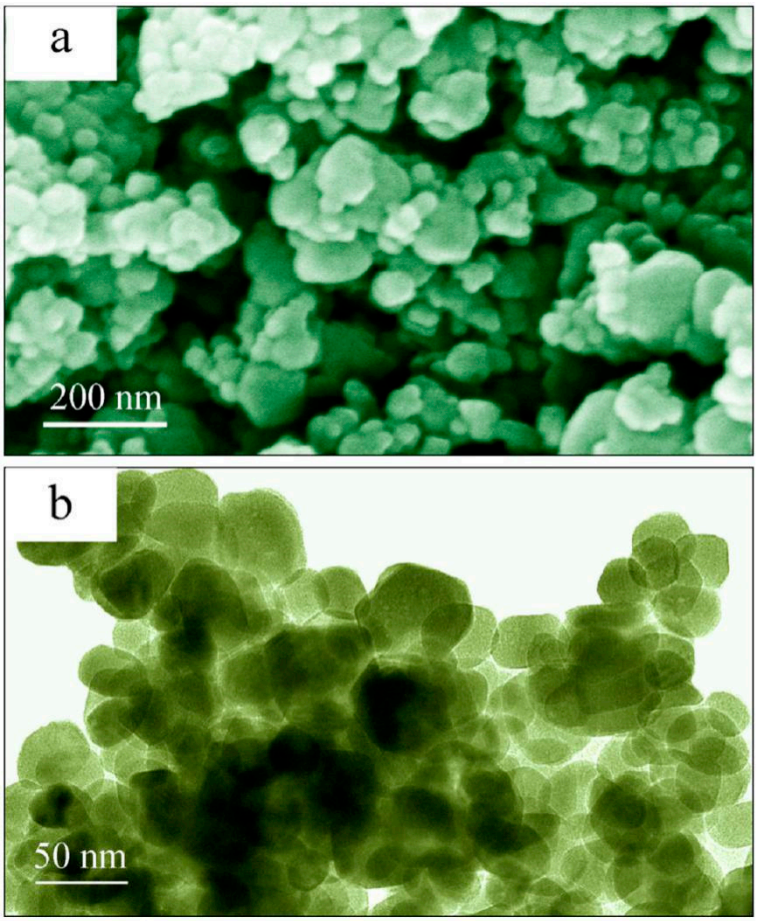

Figure 2. Microstructures of undoped ZnO nanocrystals: (**a**) scanning electron microscope (SEM) micrograph; (**b**) low-magnification transmission electron microscope (TEM) micrograph.

2.2. Absorption and Photoluminescence (PL) Spectra of ZnO Nanocrystals

We measured the diffuse reflectance spectrum of undoped ZnO nanocrystals. On the basis of the diffuse reflectance spectrum, we derived the absorption spectrum of undoped ZnO nanocrystals by making use of the method proposed by Kubelka and Munk. The ultraviolet-visible (UV-Vis) absorption spectrum of undoped ZnO nanocrystals is illustrated in Figure 3a. Obviously, undoped ZnO nanocrystals exhibit strong absorption in the ultraviolet spectral regime ($\lambda < 400$ nm). The inset of Figure 3a represents the Tauc plot and the sectional absorbance of the undoped ZnO nanocrystals. The direct bandgap of ZnO nanocrystals is found to be 3.26 eV. As mentioned before, defect-free ZnO is a semiconductor with a direct bandgap of 3.37 eV. As documented in the literature, Hamdy et al. reported that the bandgap of oxygen-defected ZnO was 3.07 eV [19]. It is obvious that our derived bandgap value of the undoped ZnO nanocrystals is closer to the well-recognized experimental values of 3.37 eV for ZnO [1,18]. The bandgap of undoped ZnO nanocrystals is too large for any photons in the visible-light regime ($\lambda > 400$ nm) to excite electrons from its valence band (VB) to its conduction band (CB). More importantly, very weak absorption at about 450 nm can be evidenced in the sectional absorbance of the undoped ZnO nanocrystals. Figure 3b illustrates the PL spectrum of undoped ZnO nanocrystals. This PL spectrum consists of a ultraviolet emission band peaking at about 380 nm and a visible emission band peaking at about 540 nm. Apparently, the ultraviolet emission band peaking at about 380 nm can be attributed to the band edge emission of ZnO whereas the visible emission band peaking at about 540 nm can be assigned to the defect emissions in ZnO. In our previous work, this visible emission band was assigned to the defect-related emissions in ZnO, particularly oxygen vacancy [3–5,12,16,17,21–23]. Electron spin resonance, a powerful technique for analyzing defects in solids, was carried out to determine the nature of these defective sites in ZnO. Using the technique of electron spin resonance, Pei et al. detected a signal at $g = 2.003$ in ZnO nanocrystals [24]. According to their report, the detected defective species are oxygen vacancies since the signal at $g = 2.003$ is commonly attributed to an unpaired electron trapped on an oxygen vacancy site [18,24]. Consequently, the data in Figure 3 have confirmed that intrinsic defects with a high concentration are present in the undoped ZnO nanocrystals, among which oxygen vacancies are a major ingredient.

2.3. PL Spectrum of the Halogen Lamp

Ultraviolet photons can break organic molecules. Thus, a visible-light illumination source is required for the reliable characterization of the visible-light photocatalytic activity of undoped ZnO nanocrystals. The PL spectrum of a 300 W halogen lamp is represented in Figure 4a. Apparently, the peak of the PL spectrum of the halogen lamp is located at about 530 nm, and the ultraviolet emissions of the lamp can be neglected. Thus, this halogen lamp serves as an ideal visible-light source. Figure 4b depicts the UV-Vis absorption spectra of methyl orange solution as a function of visible-light irradiation time in the absence of ZnO nanocrystals. As can be seen in Figure 4b, no obvious photolysis of the methyl orange can be generated when undoped ZnO nanocrystals are absent.

We checked the UV-Vis absorption spectrum of the methyl orange solution before and after the equilibrium period in the dark. Before the equilibrium period, the peak intensity of the UV-Vis absorption spectrum of the methyl orange solution decreases with the magnetic stirring time. The longer the solution is stirred, the lower the peak intensity of the UV-Vis absorption spectrum becomes. After the equilibrium period, the peak intensity of the UV-Vis absorption spectrum of the methyl orange solution reaches its minimum and keeps unchanged even if the stirring time gets longer. Before and after the equilibrium period, no obvious changes can be observed in the profile of the UV-Vis absorption spectrum of the methyl orange solution, which suggests no difference, pointing to a physical adsorption of methyl orange onto ZnO. Figure 5 depicts the UV-Vis absorption spectra of aqueous methyl orange solutions after magnetic stirring with ZnO nanocrystals for different times in the dark. As can be seen in Figure 5, the readings of the peak absorbance at 463 nm are 0.9050, 0.8220, 0.7533, 0.7274, 0.7078 and 0.7009 when the methyl orange solution is magnetically stirred with undoped ZnO nanocrystals for 0 min (the black curve), 10 min (the green curve), 20 min (the pink curve), 25 min (the cyan curve),

30 min (the blue curve) and 40 min (the dashed dark red curve), respectively. Particularly, we have noted that the blue curve is nearly overlapped with the dashed dark red curve. Consequently, the data in Figure 5 suggest that it takes about 30 min for the methyl orange molecules and the ZnO nanocrystals to establish an adsorption-desorption equilibrium.

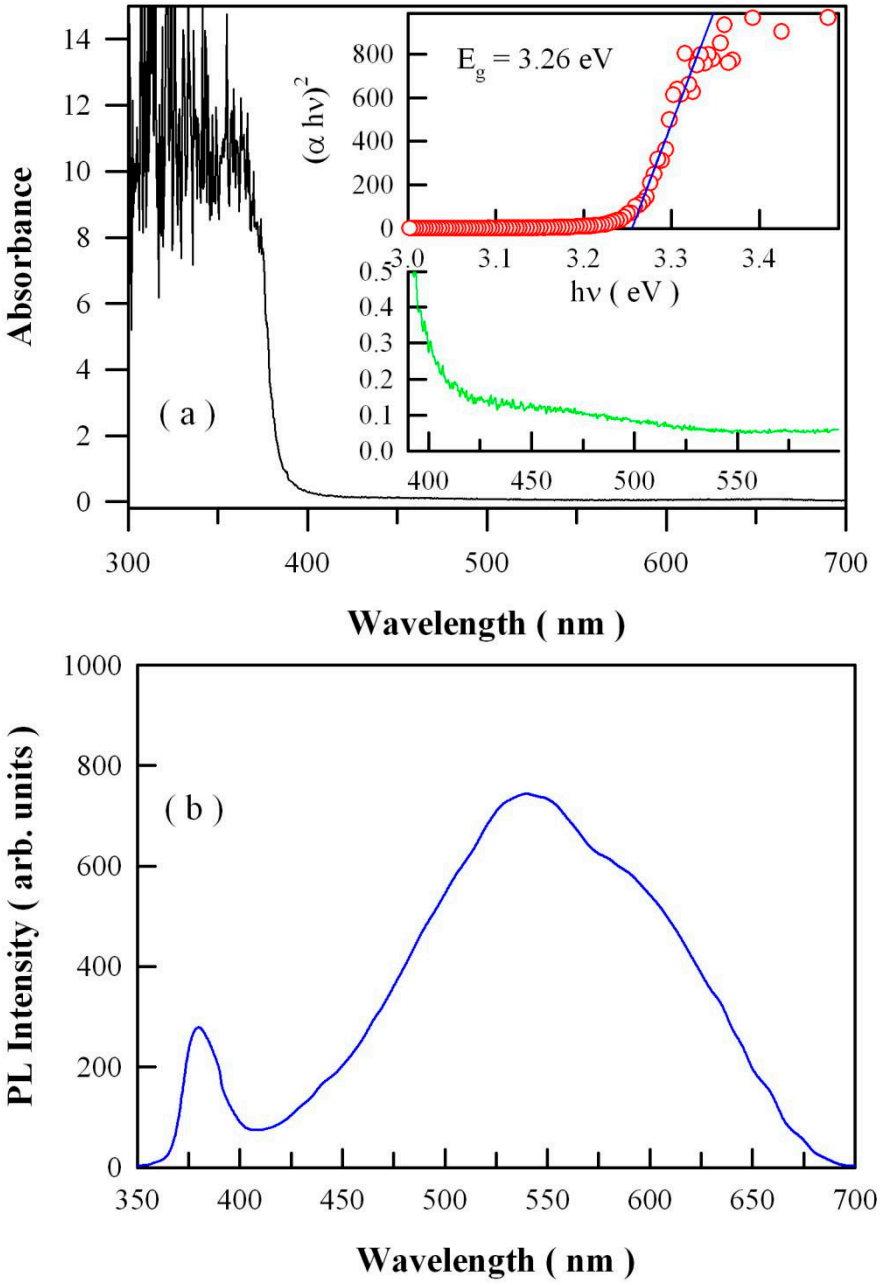

Figure 3. Ultraviolet-visible (UV-Vis) absorption spectrum (**a**) and PL spectrum (**b**) of undoped ZnO nanocrystals. Inset of (**a**): Tauc plot and sectional absorbance of the undoped ZnO nanocrystals.

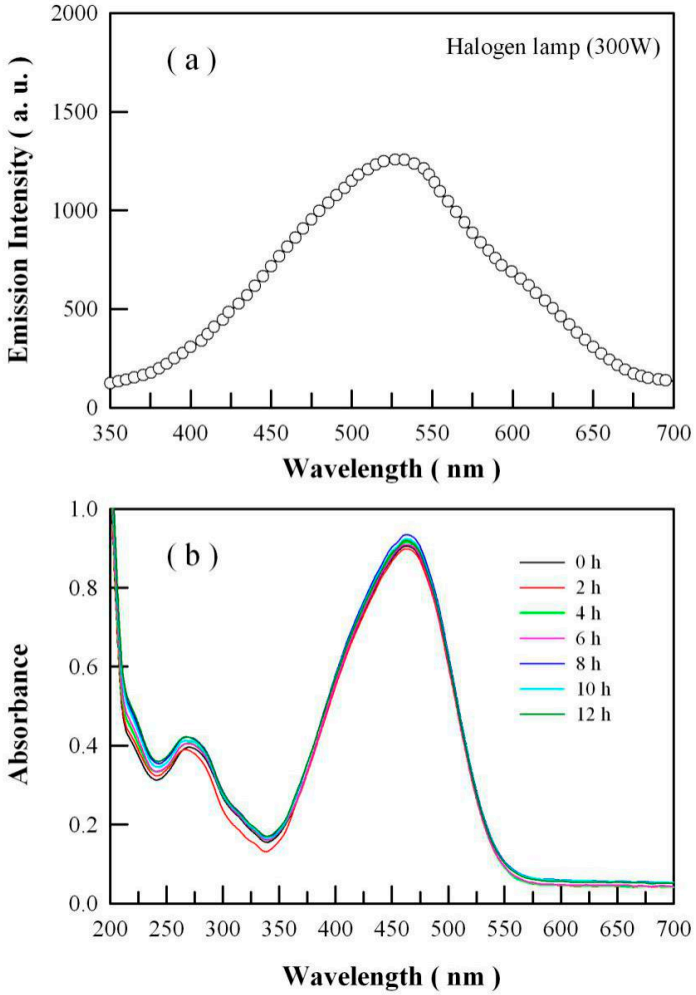

Figure 4. (**a**) Photoluminescence (PL) spectrum of a 300 W halogen lamp; (**b**) UV-Vis absorption spectra of methyl orange solution as a function of visible-light irradiation time in the absence of ZnO nanocrystals.

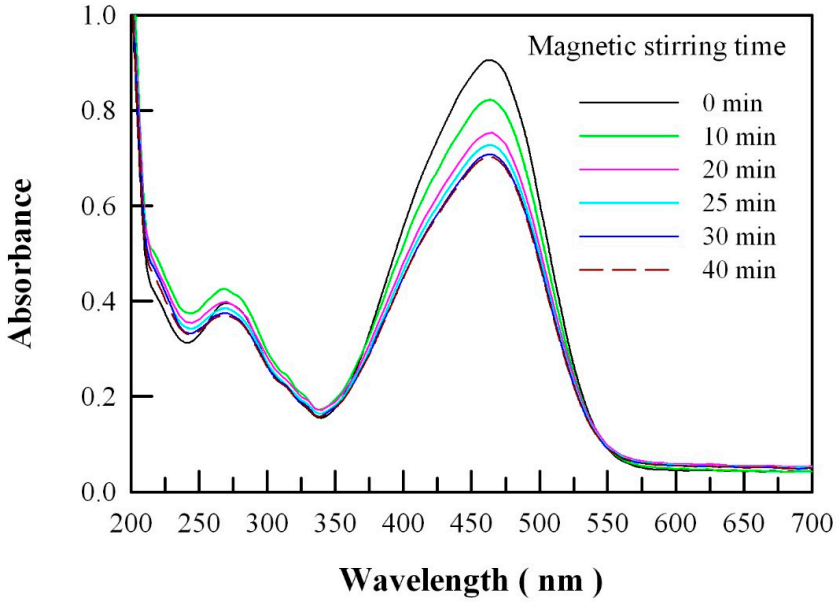

Figure 5. UV-Vis absorption spectra of aqueous methyl orange solutions after magnetic stirring with ZnO nanocrystals for different times in the dark.

2.4. Photocatalytic Activity of Undoped ZnO Nanocrystals

Figure 6a depicts the absorption spectra of photocatalytically degraded methyl orange solution under visible-light irradiation for different times. Undoped ZnO nanocrystals are the photocatalysts. As shown in Figure 6a, the intensities of the strong absorption band peaking at about 463 nm and the weak absorption band peaking at about 268 nm are decreased with the increase in the visible-light irradiation time. The simultaneous disappearance of the two absorption bands upon prolonged visible-light irradiation indicates the complete destruction of the conjugations in the methyl orange molecules. Thus, the data in Figure 6a demonstrate that undoped ZnO nanocrystals are visible-light active. Figure 6b shows the semilogarithmic plots of C_t/C_o as a function of the visible-light irradiation time in the presence of undoped ZnO nanocrystals. C_o is the initial concentration of methyl orange in water, C_t is the concentration of methyl orange in water after the visible-light irradiation time t. The linearity of the plot in Figure 6b suggests that the first-order reaction takes place during the photocatalytic degradation of methyl orange molecules. Using the technique of linear regression, the first-order rate constant is calculated to be 4.6×10^{-3} min^{-1} for the undoped ZnO nanocrystals. As documented in the literature, Pawar et al. reported that the first-order rate constant was 1.71×10^{-3} min^{-1} for commercial ZnO powders to degrade methylene blue under the visible-light illumination of a 100 W halogen lamp [7]; Hamdy et al. reported that the first-order rate constant was about 9×10^{-3} min^{-1} for commercial ZnO powders (BET surface area 22.1 m^2/g) to degrade methyl green dye under visible-light illumination of 425 ± 20 nm [19]; Wang et al. reported that the first-order rate constant was around 1×10^{-3} min^{-1} for commercial ZnO nanoparticles to degrade rhodamine B under the visible-light irradiation from a Xe lamp (8 W) equipped with an ultraviolet cutoff filter ($\lambda > 420$ nm) [20]. A rough comparison reveals that our ZnO nanocrystals exhibit reasonably high visible-light photocatalytic activity.

It is worthwhile to note that visible-light illumination is critically important for reliable characterization of the visible-light photocatalytic activity of ZnO photocatalysts. Unfortunately, some researchers tried to investigate the visible-light photocatalytic activity of ZnO nanoparticles under ultraviolet illumination. For example, Pei et al. studied the photocatalytic activity of ZnO films by photodegrading methyl orange under the illumination of ultraviolet light 365 nm [24]; Liu et al. studied the effect of native defects and photocatalytic activity of ZnO by measuring the photocatalytic activity of ZnO nanoparticles in methyl orange solution under ultraviolet illumination [25]; Fang et al. studied the effect of defects on the photocatalytic activity of ZnO nanorods under irradiation of 365 nm from a 500 W mercury lamp [26]; Wang et al. investigated the photocatalytic activity of ZnO mesocrystals under the irradiation of xenon light [27]. Although these studies suggest that native defects have an influence on the photocatalytic activities of ZnO nanostructures, the usage of ultraviolet illumination makes their conclusions shaky since ultraviolet photons can decompose the methyl orange molecules even in the absence of any photocatalysts [28]. The data of visible-light photocatalytic activity of undoped ZnO nanocrystals are reliable only when pure visible-light illumination has been utilized in the photocatalysis.

An ultraviolet blocking filter transmits much of the visible light and reflects the undesired ultraviolet energy. In order to protect the methyl orange molecules from ultraviolet damages, we employed an ultraviolet-light filter with a cut-off of 420 nm. This filter features high ultraviolet energy reflection for wavelengths less than 420 nm and excellent visible transmission for wavelengths larger than 420 nm. The maximum transmittance of the filter in the range of 300–410 nm is less than 0.5%. It was found that the undoped ZnO nanocrystals were still photocatalytically active when the ultraviolet cut-off filter was placed in front of the 300 W halogen lamp. Furthermore, the data in Figure 6 are reproduced when the ultraviolet cut-off filter is placed in front of the 300 W halogen lamp to supply visible-light illumination for the photocatalysis.

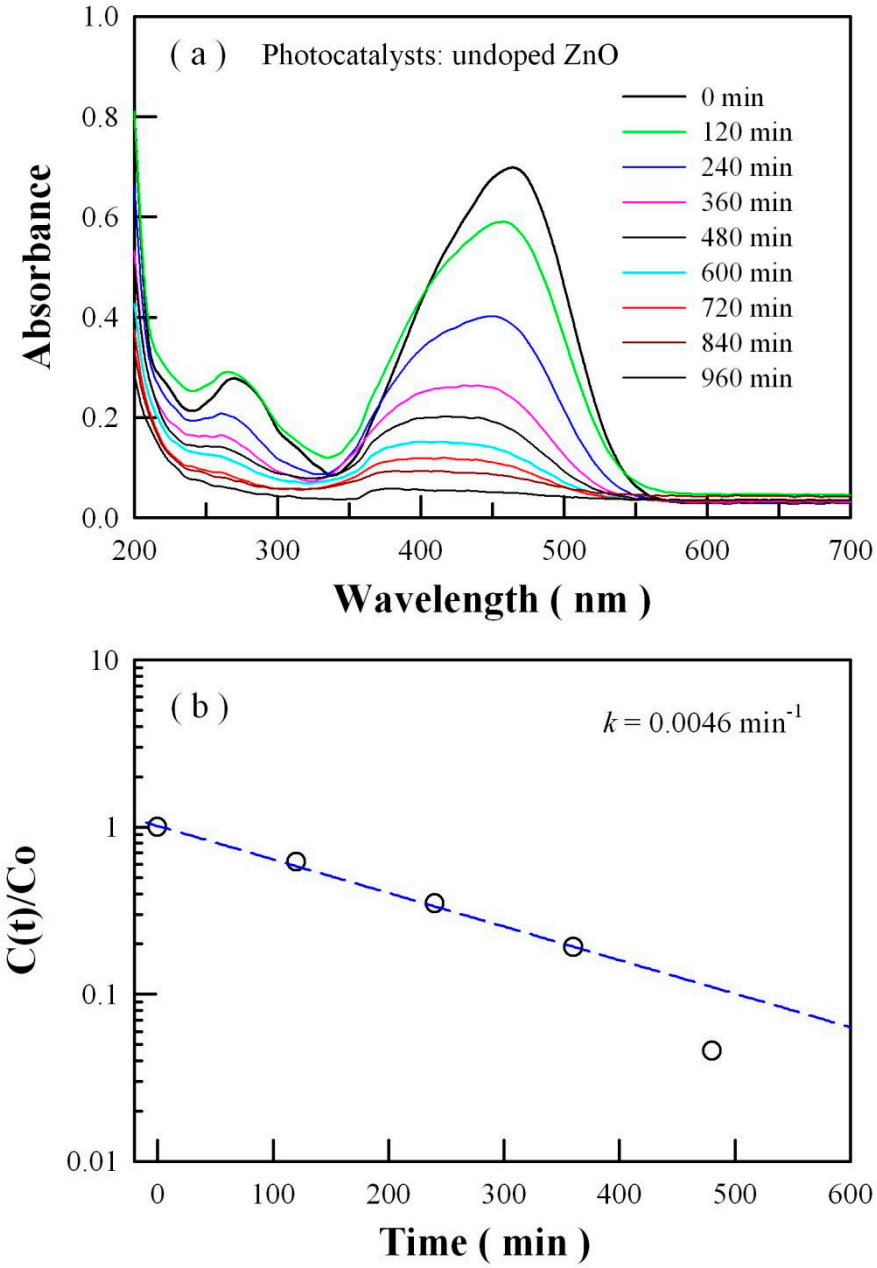

Figure 6. (**a**) UV-Vis absorption spectra of methyl orange solution as a function of visible-light irradiation time with the loading of undoped ZnO nanocrystals. (**b**) Semilogarithmic plots of Ct/Co as a function of visible-light irradiation time for undoped ZnO nanoparticles.

The visible-light photocatalytic activity of undoped ZnO nanocrystals is clearly illustrated in Figure 6. Such visible-light photocatalytic activity of undoped ZnO nanocrystals apparently originates from intrinsic defects in ZnO. Native point defects in ZnO include the oxygen and zinc vacancies, the oxygen and zinc interstitials, and the oxygen and zinc antisites. Under normal conditions, however, both the interstitials and antisites are not expected to exist in significant concentrations in ZnO because of their high formation energies [29,30]. Therefore, our discussions are focused on the oxygen and zinc vacancies, leaving the interstitials and antisites for no more consideration. The details on oxygen vacancies and zinc vacancies in ZnO were experimentally investigated using the technique of electron paramagnetic resonance [18–20,24,27,31]. For example, Hamdy et al. attributed the low-field signal with a g-factor of 2.01 to an unpaired electron trapped on an oxygen vacancy site and assigned the high-field signal with a g-factor close to 1.96 to a zinc vacancy site [19]. All the results discussed

above suggest the presence of oxygen vacancies and zinc vacancies in the undoped ZnO nanocrystals with reasonably high concentrations. Generally speaking, such vacancies can greatly influence the electronic structure and light absorption of ZnO. For instance, oxygen vacancies can create midgap states in the bandgap of $ZnWO_4$ to endow visible-light absorption to the semiconductor [32,33]. Thus, the electronic structures of ZnO with oxygen and zinc vacancies are critically important to understand the visible-light photocatalytic activity of undoped ZnO.

As can be seen in Figures 4 and 6, methyl orange is an actual light-absorbing species. The absorption spectra peaking at about 463 nm indicate that the energy difference between the highest occupied molecular orbit and the lowest unoccupied molecular orbit of methyl orange molecule is around 2.67 eV. Therefore, we have to consider the possibility of the occurrence of an energy transfer process from the methyl orange molecule to ZnO nanocrystals. Forster resonance energy transfer is a nonradiative energy transfer mechanism between an excited donor fluorophore (i.e., the methyl orange in our case) and a ground state acceptor fluorophore (i.e., the ZnO nanocrystals in our case) through dipole-dipole interactions. Three important requirements for the Forster resonance energy transfer to occur between donors and acceptors are (i) the photon emission energy of donors has to be greater than that of acceptors; (ii) the donor emission band and the acceptor absorption spectra has sufficient overlap; and (iii) the distance between donors and acceptors is within the distance limit of Forster resonance energy transfer (~10 nm). If all three requirements are met, the resonance energy transfer between donors and acceptors occurs in high probability. Unfortunately, condition (ii) is not met in our case because the methyl orange emission band has no sufficient overlap over the absorption spectrum of ZnO nanocrystals. Consequently, the energy transfer process from the methyl orange molecule to ZnO nanocrystals can be neglected.

2.5. Electronic Structures of Oxygen Deficient ZnO

Figure 7a shows the calculated band structures of defect-free ZnO. As shown in Figure 7a, defect-free ZnO exhibits a direct bandgap with a bandgap value of 3.4085 eV. The maximum of VB of defect-free ZnO is located at the point Γ, and so is the minimum of the CB of defect-free ZnO. It is clear that no midgaps are present in the bandgap of defect-free ZnO. Figure 7b shows the density functional calculated band structures of oxygen-deficient ZnO (i.e., $ZnO_{0.99}$). As shown in Figure 7b, this oxygen deficient ZnO exhibits a direct bandgap with a bandgap value of 3.5169 eV. The most prominent feature in Figure 7b is that the oxygen vacancy introduces a defect energy level in the bandgap of ZnO. This narrow defect band ranges from 0.76 to 0.82 eV with its peak at about 0.79 eV. Since the calculated bandgap (3.5169 eV) is larger than the experimental bandgap value of perfect ZnO, we have to apply the scissor operation to the derived band structures in Figure 7b. After the scissor operation, the bandgap value of $ZnO_{0.99}$ is adjusted to 3.37 eV. Correspondingly, the oxygen vacancy-introduced defect level is located at around E_V + 0.76 eV. Thus, our density functional calculations predict that the defect energy level generated by oxygen vacancies is located at E_V + 0.76 eV. Rather than a shallow donor, the data in Figure 7b show that the oxygen vacancy in ZnO is a deep donor. This viewpoint is in fairly good agreement with previous theoretical results [29,30]. The midgap states generated by the oxygen vacancies can generally act as charge traps and recombination centers. As a result, these midgap states have a significant impact on the optical absorption of oxygen deficient ZnO. According to the density functional calculations in Figure 7b, absorption of the oxygen-deficient ZnO in the visible regime can be originated from electron transition from the defect level E_V + 0.76 eV to the CB of ZnO, leading to absorption at 475 nm (2.61 eV). Obviously, we can conclude that the defect energy levels created by oxygen vacancies in the bandgap of ZnO are responsible for the visible-light absorption, which in turn leads to the visible-light photocatalytic activity of undoped ZnO nanocrystals. To this end, oxygen vacancies are responsible for the visible-light photocatalytic activity of undoped ZnO.

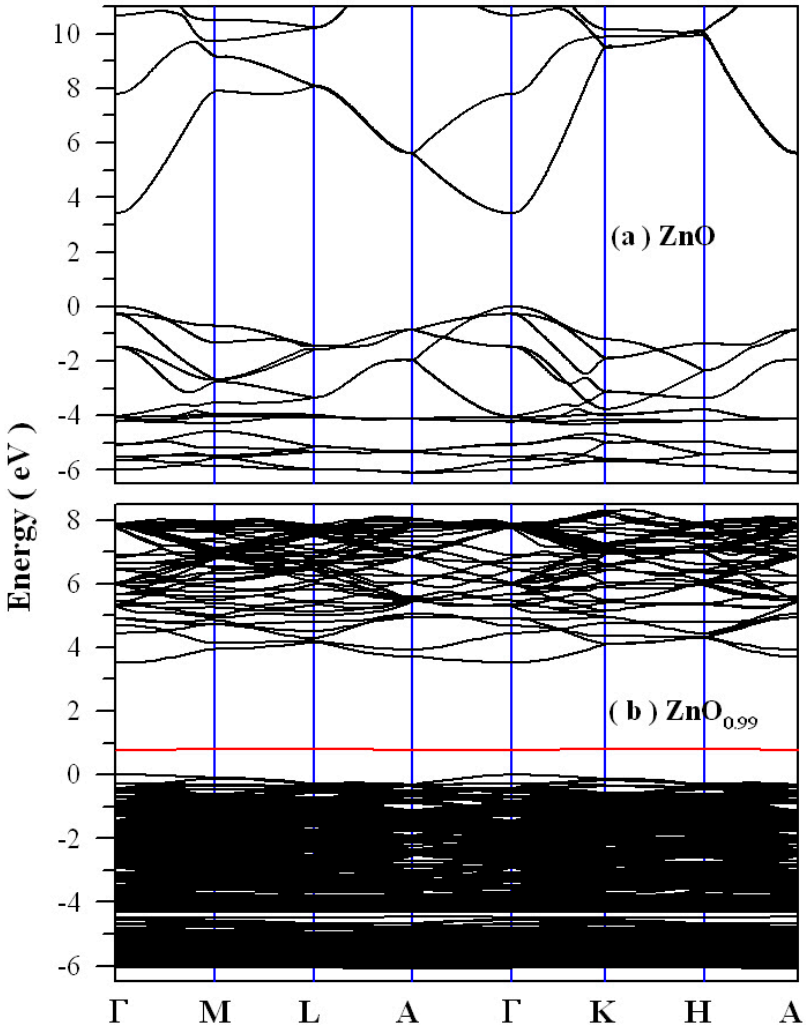

Figure 7. Density functional calculated band structures of perfect ZnO (**a**) and oxygen-deficient ZnO (**b**).

2.6. Electronic Structures of Zinc Deficient ZnO

In addition to the oxygen vacancies, the zinc vacancies may be helpful in rendering the visible-light absorption to undoped ZnO. Figure 8 shows the band structures (a) and density of states (b) of zinc-deficient ZnO (i.e., $Zn_{0.98}O$) derived via the density functional calculation. As shown by the pink curves in Figure 8, Zn vacancies generate shallow defect energy levels in the bandgap of ZnO. These defect energy levels are about 0.12 eV above the maximum of the VB. Thus, Zn vacancies are shallow acceptors. On the basis of first-principles calculations, McCluskey and Jokela also reported that some acceptor levels of zinc vacancies are 0.1–0.2 eV above the VB maximum [30]. Negatively charged zinc vacancies on the surface and in the bulk of ZnO nanocrystals can serve traps of charge carriers. Since the defect energy levels of these zinc vacancies are located at 0.12 eV above the VB, the energy required to pump electrons from Zn vacancies to the CB is estimated to be about 3.25 eV. As a result, photons with the wavelength of 382 nm will be absorbed. Apparently, such an absorption is out of the range of the visible spectral regime. Consequently, the zinc vacancies contribute nothing to the visible-light absorption of undoped ZnO nanocrystals.

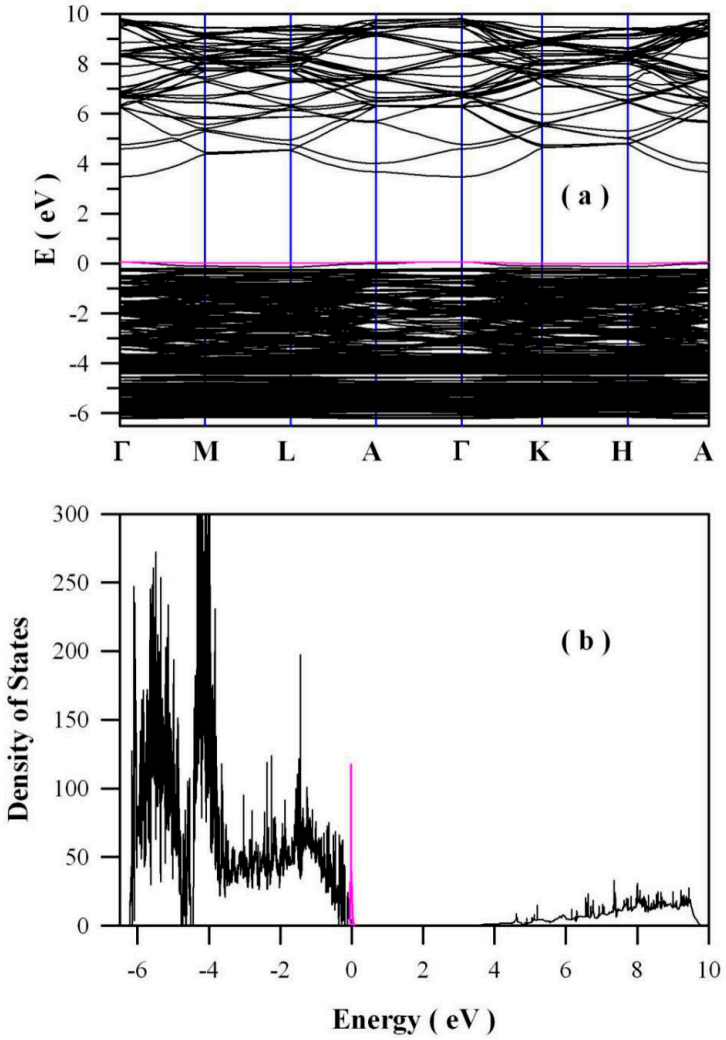

Figure 8. Band structures (**a**) and density of states (**b**) of zinc-deficient ZnO (i.e., $Zn_{0.98}O$) via the density functional calculation.

In conjunction with the electronic structures derived via density functional calculations, our results indicate that intrinsic defect engineering seems to be effective in rendering the visible-light absorption to undoped ZnO. Based on the prevailing hypothesis of oxygen vacancies, Hamdy et al. suggested that oxygen-defected ZnO could harvest more photons in the visible-light regime [19], whilst Wang et al. proposed that the surface oxygen vacancies of ZnO nanosheets could improve the visible-light absorption, which enhanced the photocatalytic activities of ZnO nanosheets under visible-light illumination [20]. Our first-principles results indicate that the midgap states of oxygen vacancies play a key role in the visible-light absorption of undoped ZnO, which in turn leads to the visible-light photocatalytic activity of undoped ZnO. Contrary to oxygen vacancies, we find that zinc vacancies are unlikely to be the cause of the visible-light photocatalytic activity of undoped ZnO. These results will be the cornerstone for the rational design of visible-light-responsive ZnO photocatalysts. Intentional manipulation of the intrinsic defect in ZnO could be an attractive possibility to design visible-light photocatalysts [34–37].

2.7. X-ray Photoelectron Spectroscopic (XPS) Spectrum of O1s in Undoped ZnO Nanocrystals

Figure 9 represents the high-resolution XPS spectrum of O1s in undoped ZnO nanocrystals. It can be seen in Figure 9 that the XPS spectral profile of O1s is peaked at 530.48 eV, but detailed analysis shows that this XPS spectrum of O1s can be deconvoluted to several Gaussian components. It is obvious that this spectrum is deconvoluted to three specific peaks: the Zn-O bond in the ZnO matrix centered at 529.92 eV (the blue curve), the oxygen vacancies centered at 530.70 eV (the green curve) and the oxygen chemical adsorption centered at 531.65 eV (the pink curve). The results of XPS also confirmed the existence of oxygen vacancy.

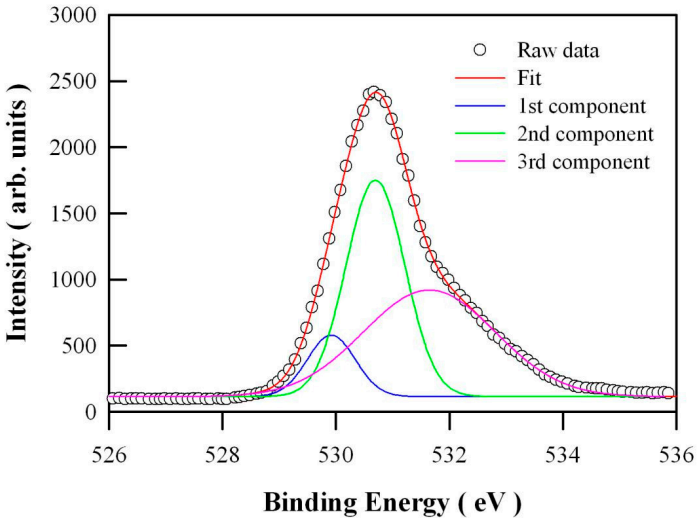

Figure 9. X-ray photoelectron spectroscopic (XPS) spectrum of O1s in undoped ZnO nanocrystals.

2.8. Visible-Light Photocatalytic Activity of Thermally-Annealed ZnO Nanocrystals

Thermal annealing can effectively modify the concentration of intrinsic defects in ZnO nanocrystals. As presented in our previous publication, the concentration of oxygen vacancies in ZnO nanocrystals increases with the annealing temperature in the range of 60–400 °C [38]. In order to evaluate the effects of the concentration of oxygen vacancies on the visible-light photocatalytic activity of undoped ZnO nanocrystals, five kinds of extra ZnO samples were prepared by thermal annealing the solution-grown ZnO nanocrystals in a box furnace at 100 °C, 150 °C, 200 °C, 250 °C and 300 °C, respectively. The duration of each annealing was 20 min. Figure 10 depicts the UV-Vis absorption spectra of aqueous methyl orange solutions after visible-light photocatalysis of thermally-annealed ZnO nanocrystals for 120 min. As can be seen in Figure 10, the visible-light photocatalytic activity of undoped ZnO nanocrystals gets higher when the undoped ZnO nanocrystals are annealed at higher temperature. This changing trend of visible-light photocatalytic activity coincides with the changing trend of the concentration of oxygen vacancies in thermally-annealed ZnO nanocrystals [38]. The data in Figure 10 indicates that the visible-light photocatalytic activity of undoped ZnO nanocrystals can be engineered via the intrinsic defects engineering.

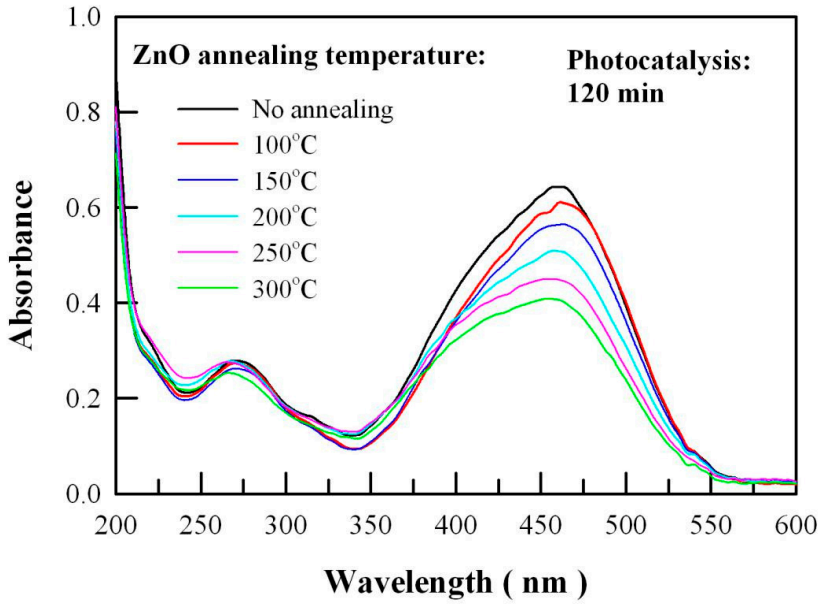

Figure 10. UV-Vis absorption spectra of aqueous methyl orange solutions after 120-min visible-light photocatalysis of thermally-annealed ZnO nanocrystals.

3. Materials, Characterizations and Calculation

Undoped ZnO nanocrystals were derived via co-precipitation synthesis. All chemicals in the wet-chemical synthesis were analytical grade reagents. They were provided by Sinopharm Chemical Reagents Ltd (Shanghai, China). 0.04 mole of $ZnCl_2$ was dissolved into 50 mL of deionized water in a flask. The aqueous solution of NaOH was prepared by dissolving NaOH (0.0864 mole) into deionized water (100 mL), which was dropped into the flask under stirring with a magnetic bar. After reacting at room temperature for 2 h, the precipitates were filtered and then washed with deionized water four times. The solids of the filtrate were dried in a vacuum oven overnight. The resulting powders were sintered in an oven at 500 °C for 3 h before any characterizations. In addition to the as-prepared ZnO sample, five kinds of extra undoped ZnO samples were prepared by thermal annealing the solution-grown ZnO nanocrystals in a box furnace at 100 °C, 150 °C, 200 °C, 250 °C and 300 °C, respectively. The duration of each annealing was 20 min.

The crystal structure of ZnO nanocrystals was characterized using XRD with an X-ray diffractometer (D/max 2500 PC, Rigaku Corporation, Akishima, Japan). The wavelength of the X-ray was 0.154 nm. The morphology of the undoped ZnO nanocrystals was analyzed with SEM made in Japan (model S-4800, Hitachi, Tokyo, Japan). The nanostructures of the sample were characterized on a TEM (JEOL JEM-2100, Japan Electronics Corp, Akishima, Japan). The XPS measurements were performed on an Escalab 250Xi spectrophotometer (Thermo Scientific, Waltham, MA, USA) with Al Kα radiation (1486.6 eV). The XPS spectrometer was calibrated by recording the binding energy of the Au4f7/2 peak at 83.9 eV. The C1s peak at 284.6 eV was taken as an internal standard. The diffuse reflectance spectrum of undoped ZnO nanocrystals was evaluated with a UV-Vis spectrophotometer (Shimadzu UV-3600, Kyoto, Japan). The PL spectrum of undoped ZnO nanocrystals was recorded with a spectrophotometer (Tianjin Gangdong Ltd., Tianjin, China). The 325-nm laser line from a helium-cadmium laser was utilized as the excitation source for the PL measurement. The output power of the laser at 325 nm was about 13 mW.

The visible-light photocatalytic activity of undoped ZnO nanocrystals was evaluated by monitoring the degradation of methyl orange in water under the visible-light irradiation of a halogen lamp (300 W). The photochemical reactor was made up of three components: an inner cylindrical quartz tube (ϕ55 mm), a cylindrical liquid container ($55 < \phi < 75$ mm), and an outer cylindrical glass tube ($75 < \phi < 140$ mm). The inner cylindrical quartz tube worked as the lamp housing with the halogen

lamp aligned along the central axis of the tube. The outer cylindrical quartz tube worked as the water circulating jacket with tape water running in it to keep the temperature of the suspension below 40 °C [5,12]. The cylindrical liquid container, which was the free space between the inner cylindrical tube and the outer cylindrical tube, was filled with 400 mL of the aqueous methyl orange solution. The initial concentration of the aqueous solution of methyl orange was about 34 mM. The ZnO catalyst loading was 400 mg. The suspension of ZnO nanocrystals in the aqueous solution of methyl orange was magnetically stirred in the dark for 30 min to establish an adsorption-desorption equilibrium. After having been exposed to visible-light irradiation for a certain period of time, 3 mL of the suspension was collected and then centrifuged to remove the photocatalysts. The concentration of the aqueous solution of methyl orange was determined by checking the absorbance of the solution on an UV-Vis spectrophotometer (UV2450, Shimazu, Kyoto, Japan).

The band structures and the density of states of undoped ZnO were derived via density functional calculations. The density functional theory package was the density functional theory module of the Quantumwise Atomistix ToolKit 11.8 (Atomistix ToolKit 11.8 package, Copenhagen, Denmark), as described in our previous work [12,39,40]. A $4 \times 4 \times 3$ supercell was constructed for the undoped ZnO. Such a supercell consisted of 96 Zn sites and 96 O sites. When one oxygen site was vacant, oxygen deficient ZnO resulted. The resultant ZnO was denoted as $ZnO_{0.99}$ in this work. Similarly, a $3 \times 3 \times 3$ supercell was constructed for the undoped ZnO. Such a supercell consisted of 54 Zn sites and 54 O sites. When one zinc site was vacant, zinc deficient ZnO resulted. The resultant ZnO was denoted as $Zn_{0.98}O$ in this work. The exchange-correlation interactions were calculated using the meta generalized gradient approximation (meta-GGA). The modified Becke and Johnson exchange potential was adopted to describe the exchange potential in the meta-GGA scheme [41,42]. The Monkhorst-Pack scheme k-points grid sampling was set at $5 \times 5 \times 5$ for the Brillouin zone. Double zeta double polarized basis sets were chosen for each element. The mesh cut-off energy was set to be 100 Hartree, and the convergence tolerance was set to be 4×10^{-5} eV for the calculations.

4. Conclusions

Undoped ZnO nanocrystals with a typical size of 50 nm in diameter were prepared via the precipitation method. Visible-light responsive photocatalytic activity of undoped ZnO nanocrystals has been evaluated under the visible-light illumination of a 300 W halogen lamp. The first-order rate constants of undoped ZnO nanocrystals to degrade methyl orange under the visible-light illumination of a 300 W halogen lamp is recorded to be 4.6×10^{-3} min^{-1}. Our first-principles calculations indicate that oxygen vacancies are deep donors, with their defect energy levels located at E_V + 0.76 eV. Meanwhile, the density functional calculations of the electronic structures illustrate that zinc vacancies are shallow acceptors, with their defect energy levels at about 0.12 eV above the maximum of VB. In conjunction with the electronic structures derived via density functional calculations, the visible-light photocatalytic activity of undoped ZnO can be attributed to the oxygen vacancies in the lattice of ZnO, since the oxygen vacancies allow ZnO to harvest more photons in the visible-light regime. Our results demonstrate that visible-light photocatalytic activity can be endowed to undoped ZnO nanocrystals by manipulating the intrinsic defects in ZnO.

Author Contributions: Data Acquisition and Formal Analysis, L.-l.C.; Writing—Original Draft Preparation, B.-g.Z.; Writing—Review & Editing, Y.M.H.; Project Administration, Y.M.H. All authors have read and agreed to the published version of the manuscript.

Funding: This research was funded by the Science and Technology Research Project of Henan Province under the grant number 182102310794, the National Natural Science Foundation of China under the grant numbers 11604028 and 11574036. The APC was funded by the Science and Technology Research Project of Henan Province under the grant number 182102310794.

Conflicts of Interest: The authors declare no conflict of interest.

References

1. Rehman, S.; Ullah, R.; Butt, A.M.; Gohar, N.D. Strategies of making TiO_2 and ZnO visible light active. *J. Hazard. Mater.* **2009**, *170*, 560–569. [CrossRef] [PubMed]
2. Zheng, Y.; Chen, C.; Zhan, Y.; Lin, X.; Zheng, Q.; Wei, K.; Zhu, J.; Zhu, Y. Luminescence and photocatalytic activity of ZnO nanocrystals: Correlation between structure and property. *Inorg. Chem.* **2007**, *46*, 6675–6682. [CrossRef] [PubMed]
3. Huang, Y.M.; Ma, Q.L.; Zhai, B.G. Core–shell Zn/ZnO structures with improved photocatalytic properties synthesized by aqueous solution method. *Funct. Mater. Lett.* **2013**, *6*, 1350058. [CrossRef]
4. Ma, Q.L.; Xiong, R.; Zhai, B.G.; Huang, Y.M. Core–shelled Zn/ZnO microspheres synthesized by ultrasonic irradiation for photocatalytic applications. *Micro Nano Lett.* **2013**, *8*, 491–495. [CrossRef]
5. Ma, Q.L.; Xiong, R.; Zhai, B.G.; Huang, Y.M. Ultrasonic synthesis of fern–like ZnO nanoleaves and their enhanced photocatalytic activity. *Appl. Surf. Sci.* **2015**, *324*, 842–848. [CrossRef]
6. Ibrahim, A.; Kumar, R.; Umar, A.; Kim, S.H.; Bumajdad, A.; Ansari, Z.A.; Baskoutas, S. Cauliflower–shaped ZnO nanomaterials for electrochemical sensing and photocatalytic applications. *Electrochim. Acta* **2016**, *222*, 463–472. [CrossRef]
7. Pawar, R.C.; Choi, D.H.; Lee, J.S.; Lee, C.S. Formation of polar surfaces in microstructured ZnO by doping with Cu and applications in photocatalysis using visible light. *Mater. Chem. Phys.* **2015**, *151*, 167–180. [CrossRef]
8. Ullah, R.; Dutta, J. Photocatalytic degradation of organic dyes with manganese–doped ZnO nanoparticles. *J. Hazard. Mater.* **2008**, *156*, 194–200. [CrossRef]
9. He, R.; Hocking, R.K.; Tsuzuki, T. Co–doped ZnO nanopowders: Location of cobalt and reduction in photocatalytic activity. *Mater. Chem. Phys.* **2012**, *132*, 1035–1040. [CrossRef]
10. Lu, Y.; Lin, Y.; Wang, D.; Wang, L.; Xie, T.; Jiang, T. A high performance cobalt–doped ZnO visible light photocatalyst and its photogenerated charge transfer properties. *Nano. Res.* **2011**, *4*, 1144–1152. [CrossRef]
11. Wang, R.; Xin, J.H.; Yang, Y.; Liu, H.; Xu, L.; Hu, J. The characteristics and photocatalytic activities of silver doped ZnO nanocrystallites. *Appl. Surf. Sci.* **2004**, *227*, 312–317. [CrossRef]
12. Zhai, B.G.; Yang, L.; Ma, Q.L.; Huang, Y.M. Visible light driven photocatalytic activity of Fe–doped ZnO nanocrystals. *Funct. Mater. Lett.* **2017**, *10*, 1750002. [CrossRef]
13. Uum, Y.R.; Han, B.S.; Lee, H.M.; Hong, S.M.; Kim, G.M.; Rhee, C.K. Magnetic and photocatalytic effect of Fe–doped nano–rod ZnO synthesized by the hydrolysis of metal powders. *Phys. Status Solidi A* **2007**, *4*, 4408–4411. [CrossRef]
14. Abed, C.; Bouzidi, C.; Elhouichet, H.; Gelloz, B.; Ferida, M. Mg doping induced high structural quality of sol–gel ZnO nanocrystals: Application in photocatalysis. *Appl. Surf. Sci.* **2015**, *349*, 855–863. [CrossRef]
15. SKhayyat, A.; Abaker, M.; Umar, A.; Alkattan, M.O.; Alharbi, N.D.; Baskoutas, S. Synthesis and characterizations of Cd–doped ZnO multipods for environmental remediation application. *J. Nanosci. Nanotechnol.* **2012**, *12*, 8453–8458. [CrossRef]
16. Huang, Y.M.; Ma, Q.L.; Zhai, B.G. A simple method to grow one–dimensional ZnO nanostructures in air. *Mater. Lett.* **2013**, *93*, 266–268. [CrossRef]
17. Huang, Y.M.; Ma, Q.L.; Zhai, B.G. Controlled morphology of ZnO nanostructures by adjusting the zinc foil heating temperature in an air–filled box furnace. *Mater. Chem. Phys.* **2014**, *147*, 788–795. [CrossRef]
18. Ischenko, V.; Polarz, S.; Grote, D.; Stavarache, V.; Fink, K.; Driess, M. Zinc oxide nanoparticles with defects. *Adv. Funct. Mater.* **2003**, *15*, 1945–1954. [CrossRef]
19. Hamdy, M.S.; Yahia, I.S.; Knoff, W.; Story, T. Oxygen–defected ZnO: Facial Synthesis and high photocatalytic performance under visible light. *Optik* **2018**, *158*, 1123–1130. [CrossRef]
20. Wang, J.; Xia, Y.; Dong, Y.; Chen, R.; Xiang, L.; Komarneni, S. Defect–rich ZnO nanosheets of high surface area as an efficient visible–light photocatalyst. *Appl. Catal. B Environ.* **2016**, *192*, 8–16. [CrossRef]
21. Ma, Q.L.; Huang, Y.M. Improved photovoltaic performance of dye sensitized solar cell by decorating TiO_2 photoanode with Li–doped ZnO nanorods. *Mater. Lett.* **2015**, *148*, 171–173. [CrossRef]
22. Ma, Q.L.; Zhai, B.G.; Huang, Y.M. Sol–gel derived ZnO/porous silicon composites for tunable photoluminescence. *J. Sol-Gel Sci. Technol.* **2012**, *64*, 110–116. [CrossRef]

23. Zhai, B.G.; Ma, Q.L.; Yang, L.; Huang, Y.M. Synthesis of morphology–tunable ZnO nanostructures via the composite hydroxide mediated approach for photocatalytic applications. *Mater. Res. Express* **2016**, *3*, 105045. [CrossRef]
24. Pei, Z.; Ding, L.; Hu, J.; Weng, S.; Zheng, Z.; Huang, M.; Liu, P. Defect and its dominance in ZnO films: A new insight into the role of defect over photocatalytic activity. *Appl. Catal. B Environ.* **2013**, *142–143*, 736–743. [CrossRef]
25. Liu, F.Z.; Guo, M.Y.; Leung, Y.H. Influence of native defects on photocatalytic activity of ZnO. *AIP Conf. Proc.* **2013**, *1566*, 75.
26. Fang, J.; Fan, H.; Ma, Y.; Wang, Z.; Chang, Q. Surface defects control for ZnO nanorods synthesized by quenching and their anti–recombination in photocatalysis. *Appl. Surf. Sci.* **2015**, *332*, 47–54. [CrossRef]
27. Wang, H.; Wang, C.; Chen, Q.; Ren, B.; Guan, R.; Cao, X.; Yang, X.; Duan, R. Interface–defect–mediated photocatalysis of mesocrystalline ZnO assembly synthesized in–situ via a template–free hydrothermal approach. *Appl. Surf. Sci.* **2017**, *412*, 517–528. [CrossRef]
28. Huang, Y.M.; Zhai, B.G.; Zhou, F.F. Effects of photo–irradiation on the optical properties and electronic structures of an azo–containing bent–core liquid crystal. *Mol. Cryst. Liq. Cryst.* **2009**, *510*, 34–42. [CrossRef]
29. Janotti, A.; van de Walle, C.G. Native point defects in ZnO. *Phys. Rev. B* **2007**, *76*, 165202. [CrossRef]
30. McCluskey, M.D.; Jokela, S.J. Defects in ZnO. *J. Appl. Phys.* **2009**, *106*, 071101. [CrossRef]
31. Kappers, L.A.; Gilliam, O.R.; Evans, S.M.; Halliburton, L.E.; Giles, N.C. EPR and optical study of oxygen and zinc vacancies in electron–irradiated ZnO. *Nucl. Instrum. Methods Phys. Res. B* **2008**, *266*, 2953. [CrossRef]
32. Zhai, B.G.; Yang, L.; Zhou, F.F.; Shi, J.S.; Huang, Y.M. Strong photo–oxidative capability of $ZnWO_4$ nanoplates with highly exposed {0–11} facets. *Catalysts* **2019**, *9*, 178. [CrossRef]
33. Huang, Y.M.; Li, M.Y.; Yang, L.; Zhai, B.G. Eu^{2+} and Eu^{3+} doubly doped $ZnWO_4$ nanoplates with superior photocatalytic performance for dye degradation. *Nanomaterials* **2018**, *8*, 765. [CrossRef] [PubMed]
34. Bai, S.; Zhang, N.; Gao, C.; Xiong, Y. Defect engineering in photocatalytic materials. *Nano Energy* **2018**, *53*, 296–336. [CrossRef]
35. Kayaci, F.; Vempati, S.; Donmez, I.; Biyikli, N.; Uyar, T. Role of zinc interstitials and oxygen vacancies of ZnO in photocatalysis: A bottom–up approach to control defect density. *Nanoscale* **2014**, *6*, 10224. [CrossRef] [PubMed]
36. Bora, T.; Sathe, P.; Laxman, K.; Dobretsov, S.; Dutta, J. Defect engineered visible light active ZnO nanorods for photocatalytic treatment of water. *Catal. Today* **2017**, *284*, 11–18. [CrossRef]
37. Baruah, S.; Rafique, R.F.; Dutta, J. Visible light photocatalysis by tailoring crystal defects in zinc oxide nanostructures. *Nano* **2008**, *3*, 399–407. [CrossRef]
38. Zhai, B.G.; Huang, Y.M. Origin of thermal–annealing induced orange emissions from solution–grown ZnO nanocrystals. *Mater. Res. Innov.* **2015**, *19*, S7-45–S7-50. [CrossRef]
39. Zhai, B.G.; Xu, H.; Zhuo, F.; Huang, Y.M. Annealing temperature dependent photoluminescence and afterglow of undoped $CaAl_2O_4$. *J. Alloys Compd.* **2020**, *821*, 153563. [CrossRef]
40. Zhai, B.G.; Yang, L.; Huang, Y.M. Intrinsic defect engineering in Eu^{3+} doped $ZnWO_4$ for annealing temperature tunable photoluminescence. *Nanomaterials* **2019**, *9*, 99. [CrossRef]
41. Tran, F.; Blaha, P. Accurate band gaps of semiconductors and insulators with a semilocal exchange–correlation potential. *Phys. Rev. Lett.* **2009**, *102*, 226401. [CrossRef] [PubMed]
42. Koller, D.; Tran, F.; Blaha, P. Merits and limits of the modified Becke–Johnson exchange potential. *Phys. Rev. B* **2011**, *83*, 195134. [CrossRef]